Micropatterned 2D Hybrid Perovskite Thin Films with Enhanced Photoluminescence Lifetimes

Kamminga, Machteld; Fang, Hong-Hua; Loi, Maria; ten Brink, Gerrit; Blake, Graeme; Palstra, Thomas; ten Elshof, Johan E.

Published in:
ACS Applied Materials & Interfaces

DOI:
10.1021/acsami.8b02236

Publication date:
2018

ACS APPLIED MATERIALS & INTERFACES

Research Article

Cite This: ACS Appl. Mater. Interfaces 2018, 10, 12878−12885

www.acsami.org

Micropatterned 2D Hybrid Perovskite Thin Films with Enhanced Photoluminescence Lifetimes

Machteld E. Kamminga,*[,†] Hong-Hua Fang,[†] Maria Antonietta Loi,[†] Gert H. ten Brink,[†] Graeme R. Blake,[†] Thomas T. M. Palstra,[†,§] and Johan E. ten Elshof*[,‡]

[†]Zernike Institute for Advanced Materials, University of Groningen, Nijenborgh 4, 9747 AG Groningen, The Netherlands

[‡]Mesa+ Institute for Nanotechnology, University of Twente, 7500 AE Enschede, The Netherlands

[§]University of Twente, Drienerlolaan 5, 7522 NB Enschede, The Netherlands

Supporting Information

ABSTRACT: The application of luminescent materials in display screens and devices requires micropatterned structures. In this work, we have successfully printed microstructures of a two-dimensional (2D), orange-colored organic/inorganic hybrid perovskite ($(C_6H_5CH_2NH_3)_2PbI_4$) using two different soft lithography techniques. Notably, both techniques yield microstructures with very high aspect ratios in the range of 1.5−1.8. X-ray diffraction reveals a strong preferential orientation of the crystallites along the *c*-axis in both patterned structures, when compared to nonpatterned, drop-casted thin films. Furthermore, (time-resolved) photoluminescence (PL) measurements reveal that the optical properties of $(C_6H_5CH_2NH_3)_2PbI_4$ are conserved upon patterning. We find that the larger grain sizes of the patterned films with respect to the nonpatterned film give rise to an enhanced PL lifetime. Thus, our results demonstrate easy and cost-effective ways to manufacture patterns of 2D organic/inorganic hybrid perovskites, while even improving their optical properties. This demonstrates the potential use of color-tunable 2D hybrids in optoelectronic devices.

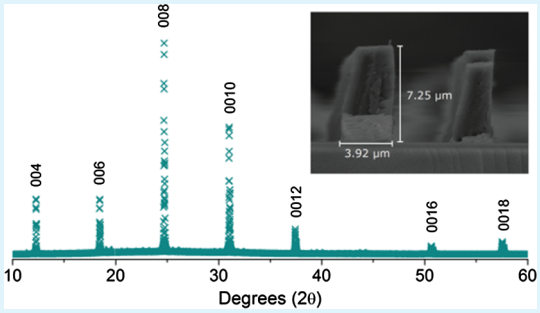

KEYWORDS: *micromolding in capillaries, imprint lithography, organic/inorganic hybrids, photoluminescence, high aspect ratio*

INTRODUCTION

Organic/inorganic hybrid perovskite materials, such as $CH_3NH_3PbI_3$, have attracted tremendous attention as promising candidates for diverse optoelectronic applications because of their unique optical[1,2] and excitonic properties,[3,4] as well as their long carrier diffusion length.[5−7] Moreover, these hybrids exhibit a wide range of tunable band gaps[8−11] and are easy to synthesize. In addition to solar light conversion,[12−16] other optoelectronic applications of this class of materials have recently been reported owing to their outstanding properties. These applications include light-emitting diodes,[17,18] field-effect transistors,[19] nonvolatile memories,[20] lasers,[21,22] and photodetectors.[23] Recently, many advances have been made to improve the quality of thin films[16,24,25] and study the effect of moisture on the film formation.[26,27] However, the application of these luminescent materials in display screens and similar devices requires patterning. This patterning should be composed of dense and uniform crystalline structures, without harming the optical properties of the materials.

The most commonly used micropatterning method in materials is photolithography, which requires complex and expensive photolithographic and etching equipment. Furthermore, a new etching procedure must be developed each time a new material is introduced. Therefore, soft lithography techniques have gained more interest as low-cost methods for creating micrometer- and submicrometer-sized structures,[28−30] in particular those that are additive techniques. These methods require a hard or an elastomeric stamp that is patterned with a relief structure on its surface. The structures can be transferred to the material by various methods, which include imprint lithography and micromolding in capillaries (MIMIC).[31] Imprint lithography is a method in which a prepatterned stamp is gently pressed into a liquid precursor film on a substrate. The MIMIC technology involves bringing a prepatterned stamp and a substrate into conformal contact to form micrometer-sized capillaries between the stamp and the substrate. After placing the precursor solution at one end of the stamp, the channels are spontaneously filled by capillary forces. Both soft lithography methods appear to be applicable for organic/inorganic hybrid perovskites,[32−34] although no direct comparison of the two methods has been made for this class of materials.

Recently, a few studies reported methods to fabricate micropatterns of the three-dimensional (3D) organic/inorganic hybrid perovskite $CH_3NH_3PbX_3$ (X = I, Br),[33−36] but only a limited amount of work has been reported on the patterning of

Received: February 6, 2018
Accepted: March 26, 2018
Published: March 26, 2018

DOI: 10.1021/acsami.8b02236
ACS Appl. Mater. Interfaces 2018, 10, 12878−12885

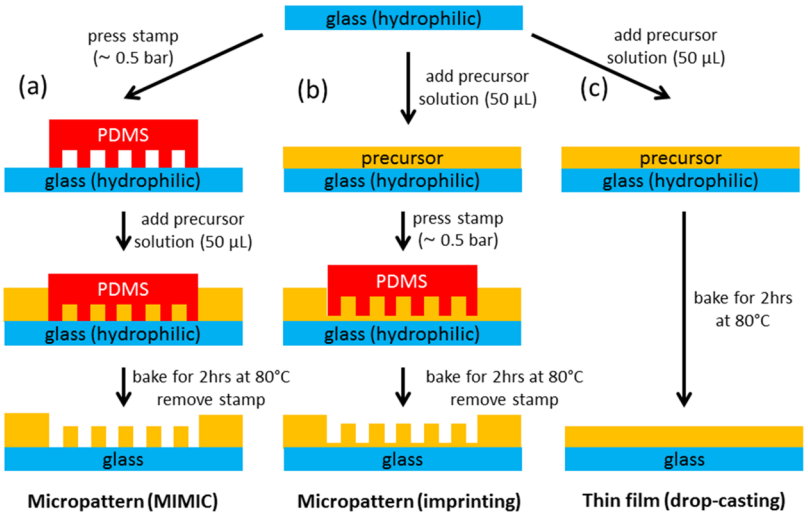

Figure 1. Schematic illustration of the patterning procedures showing two different pathways to obtain micropatterned structures: (a) MIMIC technology and (b) imprint lithography. (c) Procedure used to obtain the reference drop-casted films.

two-dimensional (2D) hybrids.[32] In most cases, 2D hybrids allow for handling under ambient conditions as they exhibit enhanced moisture stability compared to their 3D counterparts. Generally, 2D hybrid structures consist of single ⟨100⟩-terminated perovskite sheets separated by bilayers of organic cations, which are held together through van der Waals interactions.[37] Because of their quantum well structure and enhanced dielectric confinement, stable excitons with large binding energies can be formed within these materials.[38] Such high exciton binding energies are generally disadvantageous for solar cell applications, but these 2D structures can exhibit enhanced conduction within the layers[37] and have potential applications in other optoelectronic devices, such as light-emitting diodes.[17,39,40] Furthermore, 2D organic/inorganic hybrid materials allow for a large set of organic cations to be incorporated into the crystal structure and therefore for a broad range of tunable band gaps for desired applications.[10,11]

In this work, we focus on 2D benzylammonium lead iodide, $(C_6H_5CH_2NH_3)_2PbI_4$, which forms orange crystals with a direct band gap in the range of 2.12−2.19 eV.[11] We investigate and compare both imprint lithography and MIMIC technology, with which we obtain line patterns of $(C_6H_5CH_2NH_3)_2PbI_4$ with micrometer-scale resolution. Although we demonstrate the successful formation of uniform arrays of $(C_6H_5CH_2NH_3)_2PbI_4$ using both methods, the choice of method is found to have an influence on the long-range quality of the patterns. Surprisingly, X-ray diffraction (XRD) reveals that micropatterning induces a strong preferential orientation of the crystallites, as compared to nonpatterned, drop-casted films. Furthermore, photoluminescence (PL) measurements reveal that the optical properties of $(C_6H_5CH_2NH_3)_2PbI_4$ are maintained during patterning. Notably, our results show that the micropatterns contain larger grain sizes than the nonpatterned films and therefore give rise to an enhanced PL lifetime. Thus, our results demonstrate easy and cost-effective ways to manufacture patterns of 2D organic/inorganic hybrid perovskites, while maintaining their optical properties and even improving the PL lifetime. This potentially allows for the use of color-tunable 2D hybrids in optoelectronic devices.

EXPERIMENTAL SECTION

Materials Synthesis. The organic precursor salt was synthesized by slow evaporation of an equimolar mixture of HI (Sigma-Aldrich; 57 wt % in H_2O) and benzylamine (Sigma-Aldrich; 99%). After slowly adding HI to benzylamine, swirling to mix both components and heating on a hot plate at 60 °C, a white salt was formed. Once the solvent was fully evaporated, the crystallized salt was washed three times with diethyl ether (Avantor) and dried in a vacuum oven at 120 °C overnight. PbI_2 (Sigma-Aldrich; 99%) was used as the inorganic precursor. The organic/inorganic precursor solution was prepared by dissolving the organic and inorganic salts in an equimolar ratio in dimethylformamide (DMF, Sigma-Aldrich), yielding a concentration of 0.1 M.

Preparation of PDMS Stamps. A variety of 0.5 × 0.5 cm^2 polydimethylsiloxane (PDMS) stamps (around 6 mm thick) were fabricated by curing the silicone elastomer and its curing agent (Sylgard 184, Dow Corning) in a 10:1 weight ratio on a prepatterned Si master and cutting 0.5 × 0.5 cm^2 fully patterned sections out of the elastomer. The Si master used in this work contains line patterns with line widths ranging between 1 and 80 μm and a depth of 8 μm. The Si master was cleaned with a CO_2 snowjet and an oxygen plasma for 30 min and silanized before pouring PDMS over its patterned surface. To silanize the master, we used a vacuum process inspired by the work of Xia and Whitesides.[28] Here, 10 μL of trichloro(1*H*,1*H*,2*H*,2*H*-perfluorooctyl)silane (Sigma-Aldrich, 97%) was added to a desiccator containing the Si master in an argon-filled glovebox. Once brought under vacuum, silanization took place overnight, and the Si master was stored thereafter. The elastomer was degassed to remove all air bubbles, cured at 40 °C overnight, and then peeled gently off the master. Note that the cured PDMS stamps always contain some nonreacted low-molecular-weight monomers, which will slowly migrate to the surface of the stamp and leave traces on the substrate during microcontact printing or other patterning techniques. To extract the low-molecular-weight fraction, we soaked the PDMS stamps in EtOH for 6 days, before drying them on a hot plate at 50 °C for 1 h and storing in a closed box.

Patterning of the Films. The patterning of the films was performed on glass substrates by two different patterning techniques: imprint lithography and MIMIC technology. First, the glass substrates (around 2 × 2 cm^2) were cleaned with 2-propanol and then with oxygen plasma for 15 min to make the surface polar. For the imprint technique, 50 μL of the precursor solution (with a viscosity of 0.92 mPa s) was drop-casted onto the clean glass substrate, prior to slowly pressing the PDMS stamp into the precursor solution (i.e., imprinting). A home-built micromolding machine was used for perfect parallel alignment of the stamp with the substrate by applying a

DOI: 10.1021/acsami.8b02236
ACS Appl. Mater. Interfaces 2018, 10, 12878−12885

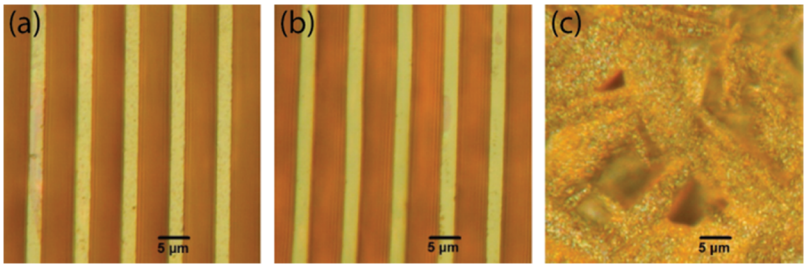

Figure 2. Optical microscopy images of micropatterned (a,b) and drop-casted thin films (c) of $(C_6H_5CH_2NH_3)_2PbI_4$. The micropatterned films were obtained by MIMIC technology (a) and imprint lithography (b). The feature size is smaller than 5 μm.

mechanical pressure of ~0.5 bar in a controlled manner. The stamps and substrates were cured under this pressure for 2 h at 80 °C. After carefully removing the stamps and removing the excess precursor, the patterned substrates were stored. For the MIMIC method, the PDMS stamp was placed directly in conformal contact with the clean substrates, with an applied pressure of ~0.5 bar. As a result, the channels of the stamp formed capillaries with the substrate. Thereafter, the precursor solution was deposited at one end of the channel-shaped stamps, and the channels were spontaneously filled by capillary forces. The stamps and substrates were cured under applied pressure for 2 h at 80 °C. After carefully removing the stamps and the excess precursor, the patterned substrates were stored.

X-ray Diffraction. XRD data were collected using a Bruker D8 ADVANCE diffractometer in Bragg–Brentano geometry and operating with Cu Kα radiation. The data were fitted using the EXPO[41] and GSAS[42] software suites.

Scanning Electron Microscopy. The microstructures were studied by scanning electron microscopy (SEM), using JEOL JSM-6490 (2.5 kV), FEI Nova NanoSEM 650 operating in a low-vacuum mode (10 and 30 kV), and Zeiss MERLIN HR-SEM (0.76 kV).

PL Measurements. PL measurements were performed at room temperature by exciting the samples at approximately 400 nm by the second harmonic of a mode-locked Ti:Sapphire laser (Mira 900, Coherent). A Hamamatsu CCD camera was used to record the PL spectra. A calibrated light source was used to correct the measurements with respect to the spectral response of the setup. Time-resolved PL (TRPL) measurements were performed with a Hamamatsu Streak camera working in a synchroscan mode.

RESULTS AND DISCUSSION

We patterned microstructures of the organic/inorganic hybrid perovskites $[(C_6H_5CH_2NH_3)_2PbI_4]$ on glass substrates using both micropatterning techniques, as illustrated in Figure 1. The glass substrates were plasma-cleaned in all cases to make them polar. For comparison, we also prepared nonpatterned thin films by drop-casting a small amount of the precursor solution (50 μL) onto a glass substrate (see Figure 1c). The precursor solution immediately spread into a uniform thin layer (of the order of 1 mm), and a polycrystalline film was obtained after thermal annealing.

As shown in Figure 1, the two micropatterning procedures differ from each other in the order in which the prepatterned PDMS stamp and the precursor solution are introduced. For the MIMIC technology, the stamp and the polar substrate are brought into conformal contact, forming capillaries between the stamp and the substrate. Once the precursor solution is introduced at one side of the stamp, the channels are spontaneously filled by capillary forces. The general advantage of this technique is that the stamp is brought into conformal contact with the substrate *before* introducing the precursor solution. Therefore, residual layers of the precursor between the patterned structures are avoided. A limiting factor for making well-defined patterns is the viscosity of the precursor solution, which should be low enough to allow a viscous flow. Moreover, a disadvantage of the MIMIC technology is that patterning isolated features is impossible.[30] Imprint lithography describes the method in which a prepatterned stamp is gently pressed onto a liquid precursor film on a substrate. Imprint lithography has the advantage over MIMIC technology that it is also applicable to solvents that do not spontaneously wet the substrate and the PDMS mold. Furthermore, isolated features can also be patterned. The main disadvantage is the possible formation of residues between the patterned structures, resulting in lower-quality structures.[30] Both patterning methods can also be applied to monomeric precursors and polymer melts, but the choice of our organic/inorganic hybrid precursor requires that both methods employ precursor solutions.

Figure 2 shows optical microscopy images of the patterned and nonpatterned films as created by the procedures illustrated in Figure 1. Both micropatterned films appear very smooth, well-defined, and uniform. The drop-casted thin film appears less smooth than the micropatterns. However, no clear distinction between the two patterning methods can be made based on the optical microscopy images alone. Figure 3 shows

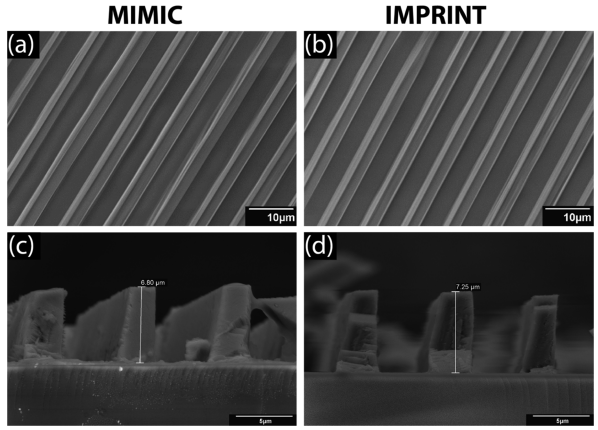

Figure 3. Top-view (a,b) and cross-sectional (c,d) SEM images of micropatterned thin films of $(C_6H_5CH_2NH_3)_2PbI_4$. The micropatterned films were obtained by MIMIC technology (a,c) and imprint lithography (b,d).

SEM images of the micropatterned structures. The top-view images in Figure 3a,b suggest that the patterned lines are of high quality, without any notable residue between the lines even for the imprinted patterns. This demonstrates that imprint lithography is a suitable method for printing organic/inorganic hybrid perovskites using DMF (solubility parameter of 12.1 $cal^{1/2}$ $cm^{-3/2}$[43]) as the solvent. This is also supported by the minimal swelling of PDMS when DMF is used as the

DOI: 10.1021/acsami.8b02236
ACS Appl. Mater. Interfaces 2018, 10, 12878–12885

solvent.[43,44] Figure S1 in the Supporting Information shows SEM images at lower magnification, covering a larger area. Here, the imprinted pattern appears very uniform over longer distances, whereas the pattern made using MIMIC technology appears to have more defects. The general quality of the MIMIC patterns is high, but this method is very sensitive to local disturbances. A single defect or obstruction in a channel will prevent the rest of the channels from becoming filled and therefore yield an incomplete pattern. Defects will only have a local influence with imprint lithography, as the precursor solution is already present everywhere in the channel before curing. Thus, MIMIC technology is based on a more dynamic process than imprint lithography and requires more parameters to be optimized to form a uniform pattern. Therefore, we reason that imprint lithography would be a more suitable method for larger-area printing than MIMIC technology. From a practical and engineering point of view, imprint lithography is hence the preferred method.

Comparison of the cross-sectional SEM images in Figure 3c,d shows different height profiles for the two patterning methods. Neither method yielded structures with a height corresponding to the channel height of the master (8 μm). The reason for this is that the channels are fully filled with the diluted liquid precursor solution, but upon drying, only a relatively small volume of the crystalline material remains. However, a simple calculation, taking into account the crystal density, the channel size, and the molarity of the precursor solution, shows that the expected pattern height in a dried channel would only be 0.27 μm. Notably, Figure 3c,d shows feature heights of 6.80 and 7.25 μm for MIMIC technology and imprint lithography, respectively. However, these are typical average feature heights, and there are some variations across different lines in each sample. The patterns made by the MIMIC method have feature heights in the range of 6 to almost 7 μm (no features were >7 μm in height), whereas the patterns made by imprint lithography have feature heights in the range of 6 to almost 7.5 μm, with several examples of features >7 μm in height. No variation in height was observed along the channel length. Note that it is not possible to use atomic force microscopy (AFM) techniques to scan the surface, as the structural features are too large.

The formation of these high structures implies that around 25× (for the 6.80 μm feature made with MIMIC technology) and 27× (for the 7.25 μm feature made with imprint lithography) more solid material accumulated in the channels than expected. Previous work on micropatterns of yttrium-stabilized zirconia, using MIMIC technology, showed that around 7.5× more solid material accumulated in the channels than that was present in the equivalent volume of the liquid precursor solution.[45] It was hypothesized that this accumulation was explained by the high permeability of the precursor solvent into the micropores of the wall of the PDMS stamp, which enabled the new precursor solution from outside the stamp to be continuously dragged into the microchannels. We reason that the same mechanism can explain the high features in both types of line patterns here. Notably, the micropatterns obtained with both techniques yielded very high aspect ratios in the range of 1.5−1.8, while well-defined objects with aspect ratios above 1 are rarely reported.[30]

We conclude that both patterning methods are suitable for generating organic/inorganic hybrid perovskite patterns, resulting in well-defined structures with very high aspect ratios. We found that imprint lithography yielded slightly higher structures and better large-scale structural uniformity. Moreover, as discussed in the Introduction, imprint lithography allows for isolated features to be patterned, whereas MIMIC technology does not. For example, microdots are typical features that are required for various applications. Another example of isolated features, that is, smiley faces, patterned by imprint lithography, is shown in Figure S2 in the Supporting Information.

Figure 4 shows the XRD profiles obtained for the micropatterned and nonpatterned films. All profiles were fitted

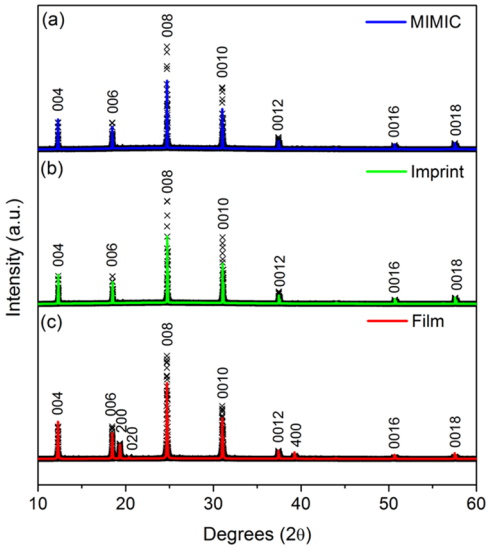

Figure 4. XRD profiles of micropatterned (a,b) and drop-casted thin films (c) of $(C_6H_5CH_2NH_3)_2PbI_4$. The micropatterned films were obtained by MIMIC technology (a) and imprint lithography (b).

using the 100 K atomic positions obtained from our previously reported single-crystal XRD data.[11] The fits incorporated the March−Dollase preferred orientation model for crystallites aligned along the *c*-axis as implemented in the GSAS software.[46] The XRD profiles confirm that both the patterned and nonpatterned films grew as a pure $(C_6H_5CH_2NH_3)_2PbI_4$ phase. However, both the imprinted and MIMIC patterns show a strong *c*-axis preferential orientation: only the 00*l* ($l = 2n$) peaks are present in the profiles. Spin-coating, a commonly employed method to deposit thin films of organic/inorganic hybrid perovskites, also generally yields highly *c*-axis-oriented films.[47] In contrast, our nonpatterned drop-casted film exhibits a lesser degree of preferential crystallite orientation, as can be seen in Figure 4. The XRD pattern of the drop-casted film shows that the film is still highly *c*-axis-oriented, as evidenced by the strong 00*l* ($l = 2n$) peaks. However, the extra peaks observed in the pattern (indexed as 200, 020, and 400) indicate that the preferred orientation is not as strong as for the micropatterned films. Spin-coating generally leads to thinner films (tens or hundreds of nanometers) than our drop-casted film. We think that spin-coated films become crystallographically oriented because the spinning gives rise to fast evaporation and concentration saturation. The spin-coating process is very fast, as the meniscus of the precursor solution is brought down at such a rate that supersaturation occurs rapidly, followed by nucleation at the energetically most favorable location, that is, at the glass substrate interface. As a result, only heterogeneous nucleation occurs, and a highly *c*-axis-oriented film is formed. In contrast, drop-casting is a much slower

DOI: 10.1021/acsami.8b02236
ACS Appl. Mater. Interfaces 2018, 10, 12878−12885

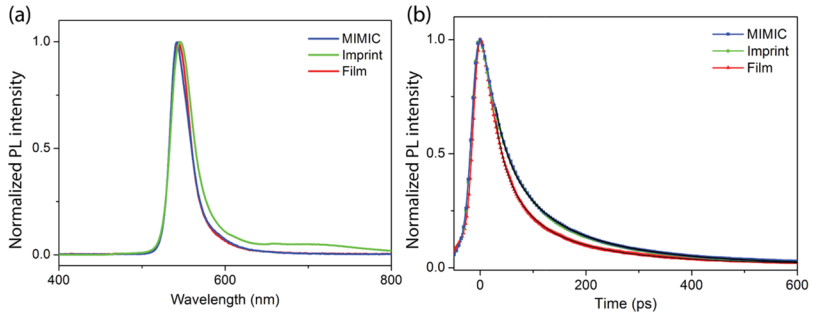

Figure 5. (a) PL and (b) TRPL spectra measured on drop-casted and micropatterned thin films, using MIMIC technology and imprint lithography, respectively, of $(C_6H_5CH_2NH_3)_2PbI_4$. The decay curves of the drop-casted and micropatterned films (made by MIMIC technology and imprint lithography) are fitted with the stretched exponential function.

technique as the precursor solution is not forced to spread as rapidly as during spin-coating. As a result, there is time for both heterogeneous and homogeneous nucleation, and the presence of homogeneous nuclei disrupts the formation of a fully oriented film, as shown in Figure 4c.

To understand the mechanism by which micropatterning yields fully *c*-axis-oriented films, we have considered various influencing factors. First, the surface/volume ratio of the confined channel does not play any role. We confirmed this by patterning lines using a PDMS stamp with 80 μm wide channels (see Figure S3 in the Supporting Information). At such low aspect ratios, the precursor solution was mainly confined by the PDMS top surface rather than by the sidewalls. Still, a fully *c*-axis-oriented pattern was obtained. Because the orientation is not dependent on the influence of the PDMS sidewalls and ceiling, it can be concluded that nucleation most likely occurs at the polar glass substrate only. Second, we hypothesize that the preferential orientation in the micropatterned structures is not caused by the drying rate. Although spin-coated films dry considerably faster than drop-casted films, we found that the micropatterns dried even more slowly than the drop-casted films while still yielding fully *c*-axis-oriented structures. The difference between the patterning and nonpatterning processes is the limited mass transport rate in the channels because of the quasi-one-dimensional (1D) confinement, and the local accumulation of mass beyond the critical nucleation concentration is therefore less likely than in a quasi-2D film. The reason is that effective diffusion rates decrease when the dimensionality is reduced.[48] The smaller mass fluxes in 1D geometries lead to smaller concentration fluctuations on the local scale, thereby lowering the chance of a nucleation event from occurring. Therefore, we infer that homogeneous nucleation is suppressed in the channels by both the physical confinement of the channel and the nonpolar nature of the PDMS stamp. As a result, highly *c*-axis-oriented patterns are formed following nucleation at the polar bottom interface. Thus, patterning not only gives rise to predefined microstructures by molding but also has a significant influence on the final orientation of the crystallites in the microstructure. We conclude that fully *c*-axis-oriented 2D organic/inorganic hybrids can be obtained by micropatterning, as an alternative to spin-coating techniques.

As stated in the Introduction, it is important that micropatterning gives rise to high-quality structures while maintaining the optical properties of the material. In Figure 5a, we show PL data from the micropatterns made using MIMIC technology and imprint lithography and from a nonpatterned, drop-casted film. The nonpatterned and patterned films yielded PL peaks at 543, 542, and 546 nm (2.28, 2.29, and 2.27 eV), respectively, which are slightly blue-shifted with respect to what we previously observed for single crystals of $(C_6H_5CH_2NH_3)_2PbI_4$ (2.12−2.19 eV).[11] Note that films and crystals are not directly comparable, as their defects and trap densities can be different, resulting in the observations of slightly different band gaps.[6] Additionally, work on related hybrid perovskites has shown great differences in quantum yield between nanocrystals and thin films.[49] However, all three films in this work were polycrystalline and had comparable band gaps. Figure 5a shows that the PL peak of the patterned film made by imprint lithography is slightly broader than those of the nonpatterned film and the patterned film made by MIMIC technology. Moreover, a shoulder is apparent at longer wavelengths. As the patterned films made by MIMIC technology generally have fewer problems with the residues between the patterned features than the patterned films made by imprint lithography, we attribute this difference in the optical properties to the presence of more defects and vacancies in the imprinted film. The presence of defects and vacancies drives recombination in these systems and can result in interstitial bands that give rise to transitions at lower energy. Moreover, strong electron-vibration coupling effects in the deformable lattice and correlated self-trapped states play a role. In fact, broadband, white-light PL has recently been shown in a series of related 2D perovskite single crystals.[50−52] Note that the patterned films made by MIMIC technology are of high quality, but that the large-area application of MIMIC technology is limited, as discussed above.

Figure 5b shows the corresponding TRPL spectra. Notably, the micropatterned films appear to have longer lifetimes than the nonpatterned film. From the graph, it is very clear that the MIMIC and the imprint spectra are nearly identical, but they clearly differ from the nonpatterned film. We found that the decay curves cannot be fitted with a monoexponential curve, as the decay appears more complex. The best way to deal with the multiexponential decay in our material, without overparameterizing, is by fitting with a stretched exponential (Kohlrausch[53]) function.[54,55] The stretched exponential function $F(t)$ is given by

$$F(t) = F_0 \exp\left[-\left(\frac{t}{\tau_0}\right)^{\beta}\right]$$

where τ_0 is the effective time constant and β (a constant between 0 and 1) is the stretch parameter that is a direct measure for the local heterogeneity of the sample, which is

DOI: 10.1021/acsami.8b02236
ACS Appl. Mater. Interfaces 2018, 10, 12878−12885

related to the width of the lifetime distribution. However, following the work of Zatryb et al.[55] on PL decay, in our experiment, we did not measure the relaxation function directly. Instead, we measured the number of photons that are emitted in a very short time period after the excitation pulse. This number of photons is directly proportional to the change of the population of the excited emitters. Therefore, the decay of the PL intensity is given by a negative time derivative of the relaxation function, and hence, the stretched exponential function for PL decay becomes

$$I_{PL}(t) = C \cdot t^{\beta-1} \exp\left[-\left(\frac{t}{\tau_0}\right)^{\beta}\right]$$

where C is a constant. Figure 5b shows the fits using the following fitting parameters: τ_0 = 79 ps and β = 0.57 for the drop-casted thin film and τ_0 = 113 ps and β = 0.69 and τ_0 = 115 ps and β = 0.68 for the micropatterned films, made by MIMIC technology and imprint lithography, respectively. The average decay time constant τ can be determined by

$$\tau = \frac{\tau_0}{\beta}\Gamma\left(\frac{1}{\beta}\right)$$

where Γ is the gamma function. The average decay time constants are 127 ps for the nonpatterned film and 149 and 145 ps for the micropatterned films, made by MIMIC technology and imprint lithography, respectively. Thus, the PL lifetimes of the micropatterned films are nearly identical and enhanced with respect to the nonpatterned film.

Figure 6a shows the 008 XRD peak ($K\alpha_1/K\alpha_2$ doublet) of the three samples. The peak width of the micropatterned films

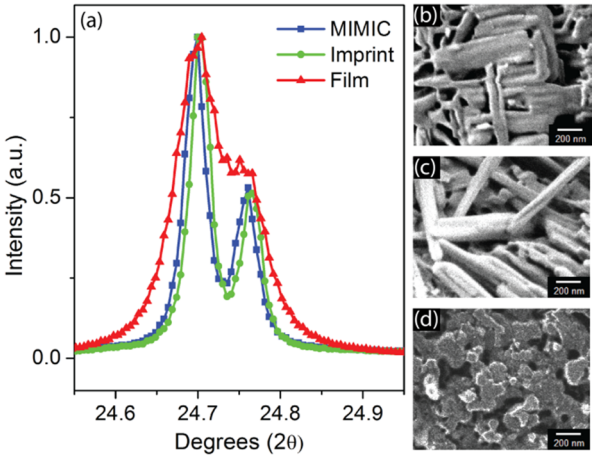

Figure 6. (a) 008 XRD peaks ($K\alpha_1/K\alpha_2$ doublet) for drop-casted and micropatterned films. (b–d) SEM images of (micropatterned) thin films made by MIMIC technology, imprint lithography, and drop-casting.

is significantly smaller than that of the nonpatterned film. This implies that the patterned films have larger crystallites than the nonpatterned films. As shown in Figure 6b–d, the nonpatterned films indeed have significantly smaller crystallites than the patterned films (bar-shaped crystallites). We believe that these small crystallites are formed by homogeneous nucleation and that they are responsible for the less oriented nature of these films. The small features also explain the longer lifetime of the patterned films, as larger crystallites exhibit a smaller radiative recombination coefficient, resulting in longer PL lifetimes.[56,57] Because the slow drying process facilitates both homogeneous and heterogeneous nucleation events, a high concentration of nucleation points and hence small crystallites are obtained in the nonpatterned film. In the patterned structures, however, mass transport can occur in a 1D fashion because of the geometry of the channels. The MIMIC and imprint processes differ dynamically. At the moment the stamp is brought into contact with the precursor, the dynamical processes for MIMIC and imprint are not the same. However, crystallization occurs sometime after penetration has taken place or the stamp is brought into conformal contact with the substrate. At that moment, MIMIC and imprint are comparable as they both represent a stagnant situation in which no pressure-driven flow occurs and only 1D diffusional transport along the channel can occur while crystallization takes place. In this situation, fewer conflicting nucleation centers form and the material can be transported over longer distances, feeding nuclei and allowing the growth of larger grains. We conclude that micropatterning not only maintains the optical properties of $(C_6H_5CH_2NH_3)_2PbI_4$ but also enhances slightly the PL lifetime compared to nonpatterned, drop-casted films. The fact that the lifetime enhancement is the largest when MIMIC technology is used demonstrates an advantage of MIMIC technology over imprint lithography. However, the variation of the lifetime is rather small.

CONCLUSIONS

We have investigated two different soft lithography methods to obtain line patterns of $(C_6H_5CH_2NH_3)_2PbI_4$ with high resolution: imprint lithography and MIMIC technology. Our results show the successful formation of uniform arrays of high-aspect-ratio (well above 1.5) $(C_6H_5CH_2NH_3)_2PbI_4$ micropatterns using both methods. Although we find both methods to be applicable for the micropatterning of our organic/inorganic hybrid, the choice of method does have an influence on the characteristics of the patterns formed. Imprint lithography yields patterns with slightly higher features and better large-scale uniformity. Moreover, isolated features can be made with imprint lithography. MIMIC technology is based on a more dynamic process than imprint lithography and requires more parameters to be optimized to form a uniform pattern.

Because the XRD data demonstrate that micropatterning induces a strong preferential orientation of the crystallites compared to nonpatterned, drop-casted films, we conclude that fully *c*-axis-oriented 2D organic/inorganic hybrids can be obtained by micropatterning, as an alternative to spin-coating techniques. Furthermore, our (TR)PL measurements reveal that the optical properties of $(C_6H_5CH_2NH_3)_2PbI_4$ are maintained during patterning. Notably, the larger grain size obtained by patterning gives rise to an enhanced PL lifetime compared to nonpatterned drop-casted films. Thus, we have explored easy and cost-effective ways to manufacture patterns of 2D organic/inorganic hybrid perovskites, while maintaining and even enhancing their optical properties, and we find that the patterning technique used has an influence on the microstructure and therefore the optical properties of the films. This allows for the implementation of color-tunable 2D hybrid novel optoelectronic devices.

DOI: 10.1021/acsami.8b02236
ACS Appl. Mater. Interfaces 2018, 10, 12878–12885

■ ASSOCIATED CONTENT

Supporting Information

The Supporting Information is available free of charge on the ACS Publications website at DOI: 10.1021/acsami.8b02236.

SEM images, optical microscopy images, and powder XRD data of imprinted $(C_6H_5CH_2NH_3)_2PbI_4$ thin films (PDF)

■ AUTHOR INFORMATION

Corresponding Authors

*E-mail: m.e.kamminga@rug.nl (M.E.K.).
*E-mail: j.e.tenelshof@utwente.nl (J.E.t.E.).

ORCID

Machteld E. Kamminga: 0000-0002-3071-6996
Maria Antonietta Loi: 0000-0002-7985-7431
Graeme R. Blake: 0000-0001-9531-7649
Thomas T. M. Palstra: 0000-0001-5239-3115
Johan E. ten Elshof: 0000-0001-7995-6571

Notes

The authors declare no competing financial interest.

■ ACKNOWLEDGMENTS

M.E.K. was supported by The Netherlands Organisation for Science NWO (Graduate Programme 2013, no. 022.005.006). We thank M.A. Smithers for SEM work and D. Cunha, S. Zhou, and M. Salverda for their AFM work. We also thank K. van den Nieuwenhuizen and D. Post for technical support.

■ REFERENCES

(1) Papavassiliou, G. C. Synthetic three- and lower-dimensional semiconductors based on inorganic units. *Mol. Cryst. Liq. Cryst.* **1996**, *286*, 231−238.

(2) Mitzi, D. B. Synthesis, Crystal Structure, and Optical and Thermal Properties of $(C_4H_9NH_3)_2MI_4$ (M = Ge, Sn, Pb). *Chem. Mater.* **1996**, *8*, 791−800.

(3) Tanaka, K.; Takahashi, T.; Ban, T.; Kondo, T.; Uchida, K.; Miura, N. Comparative study on the excitons in lead-halide-based perovskite-type crystals $CH_3NH_3PbBr_3$ $CH_3NH_3PbI_3$. *Solid State Commun.* **2003**, *127*, 619−623.

(4) Fang, H.-H.; Raissa, R.; Abdu-Aguye, M.; Adjokatse, S.; Blake, G. R.; Even, J.; Loi, M. A. Photophysics of Organic-Inorganic Hybrid Lead Iodide Perovskite Single Crystals. *Adv. Funct. Mater.* **2015**, *25*, 2378−2385.

(5) Stranks, S. D.; Eperon, G. E.; Grancini, G.; Menelaou, C.; Alcocer, M. J. P.; Leijtens, T.; Herz, L. M.; Petrozza, A.; Snaith, H. J. Electron-hole diffusion lengths exceeding 1 micrometer in an organometal trihalide perovskite absorber. *Science* **2013**, *342*, 341−344.

(6) Dong, Q.; Fang, Y.; Shao, Y.; Mulligan, P.; Qiu, J.; Cao, L.; Huang, J. Electron-hole diffusion lengths > 175 mm in solution-grown $CH_3NH_3PbI_3$ single crystals. *Science* **2015**, *347*, 967−970.

(7) Xing, G.; Mathews, N.; Sun, S.; Lim, S. S.; Lam, Y. M.; Grätzel, M.; Mhaisalkar, S.; Sum, T. C. Long-range balanced electron- and hole-transport lengths in organic-inorganic $CH_3NH_3PbI_3$. *Science* **2013**, *342*, 344−347.

(8) Eperon, G. E.; Stranks, S. D.; Menelaou, C.; Johnston, M. B.; Herz, L. M.; Snaith, H. J. Formamidinium lead trihalide: a broadly tunable perovskite for efficient planar heterojunction solar cells. *Energy Environ. Sci.* **2014**, *7*, 982−988.

(9) Noh, J. H.; Im, S. H.; Heo, J. H.; Mandal, T. N.; Seok, S. Il. Chemical Management for Colorful, Efficient, and Stable Inorganic−Organic Hybrid Nanostructured Solar Cells. *Nano Lett.* **2013**, *13*, 1764−1769.

(10) Filip, M. R.; Eperon, G. E.; Snaith, H. J.; Giustino, F. Steric engineering of metal-halide perovskites with tunable optical band gaps. *Nat. Commun.* **2014**, *5*, 5757.

(11) Kamminga, M. E.; Fang, H.-H.; Filip, M. R.; Giustino, F.; Baas, J.; Blake, G. R.; Loi, M. A.; Palstra, T. T. M. Confinement Effects in Low-Dimensional Lead Iodide Perovskite Hybrids. *Chem. Mater.* **2016**, *28*, 4554−4562.

(12) Chen, Q.; Zhou, H.; Hong, Z.; Luo, S.; Duan, H.-S.; Wang, H.-H.; Liu, Y.; Li, G.; Yang, Y. Planar heterojunction perovskite solar cells via vapor assisted solution process. *J. Am. Chem. Soc.* **2014**, *136*, 622−625.

(13) Liu, D.; Kelly, T. L. Perovskite solar cells with a planar heterojunction structure prepared using room-temperature solution processing techniques. *Nat. Photonics* **2013**, *8*, 133−138.

(14) Liu, M.; Johnston, M. B.; Snaith, H. J. Efficient planar heterojunction perovskite solar cells by vapour deposition. *Nature* **2013**, *501*, 395−398.

(15) Ke, W.; Fang, G.; Wan, J.; Tao, H.; Liu, Q.; Xiong, L.; Qin, P.; Wang, J.; Lei, H.; Yang, G.; Qin, M.; Zhao, X.; Yan, Y. Efficient hole-blocking layer-free planar halide perovskite thin-film solar cells. *Nat. Commun.* **2015**, *6*, 6700.

(16) Zhang, W.; Saliba, M.; Moore, D. T.; Pathak, S. K.; Hörantner, M. T.; Stergiopoulos, T.; Stranks, S. D.; Eperon, G. E.; Alexander-Webber, J. A.; Abate, A.; Sadhanala, A.; Yao, S.; Chen, Y.; Friend, R. H.; Estroff, L. A.; Wiesner, U.; Snaith, H. J. Ultrasmooth organic−inorganic perovskite thin-film formation and crystallization for efficient planar heterojunction solar cells. *Nat. Commun.* **2015**, *6*, 6142.

(17) Tan, Z.-K.; Moghaddam, R. S.; Lai, M. L.; Docampo, P.; Higler, R.; Deschler, F.; Price, M.; Sadhanala, A.; Pazos, L. M.; Credgington, D.; Hanusch, F.; Bein, T.; Snaith, H. J.; Friend, R. H. Bright light-emitting diodes based on organometal halide perovskite. *Nat. Nanotechnol.* **2014**, *9*, 687−692.

(18) Zhang, F.; Zhong, H.; Chen, C.; Wu, X.; Hu, X.; Huang, H. Brightly Luminescent and Color-tunable colloidal $CH_3NH_3PbX_3$ (X = Br, I, Cl) Quantum Dots: Potential Alternatives for Display Technology. *ACS Nano* **2015**, *9*, 4533−4542.

(19) Chin, X. Y.; Cortecchia, D.; Yin, J.; Bruno, A.; Soci, C. Lead iodide perovskite light-emitting field-effect transistor. *Nat. Commun.* **2015**, *6*, 7383.

(20) Yoo, E. J.; Lyu, M.; Yun, J.-H.; Kang, C. J.; Choi, Y. J.; Wang, L. Resistive Switching Behavior in Organic-Inorganic Hybrid $CH_3NH_3PbI_{3-x}Cl_x$ Perovskite for Resistive Random Access Memory Devices. *Adv. Mater.* **2015**, *27*, 6170−6175.

(21) Xing, G.; Mathews, N.; Lim, S. S.; Yantara, N.; Liu, X.; Sabba, D.; Grätzel, M.; Mhaisalkar, S.; Sum, T. C. Low-temperature solution-processed wavelength-tunable perovskites for lasing. *Nat. Mater.* **2014**, *13*, 476−480.

(22) Zhu, H.; Fu, Y.; Meng, F.; Wu, X.; Gong, Z.; Ding, Q.; Gustafsson, M. V.; Trinh, M. T.; Jin, S.; Zhu, X.-Y. Lead halide perovskite nanowire lasers with low lasing thresholds and high quality factors. *Nat. Mater.* **2015**, *14*, 636−642.

(23) Fang, Y.; Dong, Q.; Shao, Y.; Yuan, Y.; Huang, J. Highly narrowband perovskite single-crystal photodetectors enabled by surface-charge recombination. *Nat. Photonics* **2015**, *9*, 679−686.

(24) Heo, J. H.; Song, D. H.; Im, S. H. Planar $CH_3NH_3PbBr_3$ Hybrid Solar Cells with 10.4% Power Conversion Efficiency, Fabricated by Controlled Crystallization in the Spin-Coating Process. *Adv. Mater.* **2014**, *26*, 8179−8183.

(25) Nie, W.; Tsai, H.; Asadpour, R.; Blancon, J.-C.; Neukirch, A. J.; Gupta, G.; Crochet, J. J.; Chhowalla, M.; Tretiak, S.; Alam, M. A.; Wang, H.-L.; Mohite, A. D. High-efficiency solution-processed perovskite solar cells with millimeter-scale grains. *Science* **2015**, *347*, 522−525.

(26) You, J.; Yang, Y.; Hong, Z.; Song, T.-B.; Meng, L.; Liu, Y.; Jiang, C. Moisture assisted perovskite film growth for high performance solar cells. *Appl. Phys. Lett.* **2014**, *105*, 183902.

(27) Eperon, G. E.; Habisreutinger, S. N.; Leijtens, T.; Bruijnaers, B. J.; Van Franeker, J. J.; deQuilettes, D. W.; Pathak, S.; Sutton, R. J.; Grancini, G.; Ginger, D. S.; Janssen, R. A. J.; Petrozza, A.; Snaith, H. J.

DOI: 10.1021/acsami.8b02236
ACS Appl. Mater. Interfaces 2018, 10, 12878−12885

The Importance of Moisture in Hybrid Lead Halide Perovskite Thin Film Fabrication. *ACS Nano* **2015**, *9*, 9380−9393.
(28) Xia, Y.; Whitesides, G. M. Soft lithography. *Annu. Rev. Mater. Sci.* **1998**, *28*, 153−184.
(29) Seraji, S.; Wu, Y.; Jewell-larson, N. E.; Forbess, M. J.; Limmer, S. J.; Chou, T. P.; Cao, G. Patterned Microstructure of Sol-Gel Derived Complex Oxides Using Soft Lithography. *Adv. Mater.* **2000**, *19*, 1421−1424.
(30) ten Elshof, J. E.; Khan, S. U.; Göbel, O. F. Micrometer and nanometer-scale parallel patterning of ceramic and organic-inorganic hybrid materials. *J. Eur. Ceram. Soc.* **2010**, *30*, 1555−1577.
(31) Kim, E.; Xia, Y.; Whitesides, G. M. Micromolding in Capillaries: Applications in Materials Science. *J. Am. Chem. Soc.* **1996**, *118*, 5722−5731.
(32) Cheng, Z. Y.; Wang, Z.; Xing, R. B.; Han, Y. C.; Lin, J. Patterning and photoluminescent properties of perovskite-type organic/inorganic hybrid luminescent films by soft lithography. *Chem. Phys. Lett.* **2003**, *376*, 481−486.
(33) Jeong, B.; Hwang, I.; Cho, S. H.; Kim, E. H.; Cha, S.; Lee, J.; Kang, H. S.; Cho, S. M.; Choi, H.; Park, C. Solvent-Assisted Gel Printing for Micropatterning Thin Organic-Inorganic Hybrid Perovskite Films. *ACS Nano* **2016**, *10*, 9026−9035.
(34) Wu, J.; Chen, J.; Zhang, Y.; Xu, Z.; Zhao, L.; Liu, T.; Luo, D.; Yang, W.; Chen, K.; Hu, Q.; Ye, F.; Wu, P.; Zhu, R.; Gong, Q. Pinhole-Free Hybrid Perovskite Film with Arbitrarily-Shaped Micro- Patterns for Functional Optoelectronic Devices. *Nano Lett.* **2017**, *17*, 3563−3569.
(35) Feng, J.; Yan, X.; Zhang, Y.; Wang, X.; Wu, Y.; Su, B.; Fu, H.; Jiang, L. "Liquid Knife" to Fabricate Patterning Single-Crystalline Perovskite Microplates toward High-Performance Laser Arrays. *Adv. Mater.* **2016**, *28*, 3732−3741.
(36) Wang, G.; Li, D.; Cheng, H.-C.; Li, Y.; Chen, C.-Y.; Yin, A.; Zhao, Z.; Lin, Z.; Wu, H.; He, Q.; Ding, M.; Liu, Y.; Huang, Y.; Duan, X. Wafer-scale growth of large arrays of perovskite microplate crystals for functional electronics and optoelectronics. *Sci. Adv.* **2015**, *1*, No. e1500613.
(37) Mitzi, D. B.; Wang, S.; Feild, C. A.; Chess, C. A.; Guloy, A. M. Conducting Layered Organic-inorganic Halides Containing <110>-Oriented Perovskite Sheets. *Science* **1995**, *267*, 1473−1476.
(38) Takeoka, Y.; Fukasawa, M.; Matsui, T.; Kikuchi, K.; Rikukawa, M.; Sanui, K. Intercalated formation of two-dimensional and multilayered perovskites in organic thin films. *Chem. Commun.* **2005**, 378−380.
(39) Kim, Y.-H.; Cho, H.; Heo, J. H.; Kim, T.-S.; Myoung, N.; Lee, C.-L.; Im, S. H.; Lee, T.-W. Multicolored Organic/Inorganic Hybrid Perovskite Light-Emitting Diodes. *Adv. Mater.* **2015**, *27*, 1248−1254.
(40) Xiao, Z.; Kerner, R. A.; Zhao, L.; Tran, N. L.; Lee, K. M.; Koh, T.-W.; Scholes, G. D.; Rand, B. P. Efficient perovskite light-emitting diodes featuring nanometre-sized crystallites. *Nat. Photonics* **2017**, *11*, 108−115.
(41) Altomare, A.; Camalli, M.; Cuocci, C.; Giacovazzo, C. EXPO2009: structure solution by powder data in direct and reciprocal space. *J. Appl. Crystallogr.* **2009**, *42*, 1197−1202.
(42) Larson, A. C.; Von Dreele, R. B. General Structure Analysis System (GSAS). Los Alamos National Laboratory Report LAUR 86-748 2004, *86*, 1−224.
(43) Lee, J. N.; Park, C.; Whitesides, G. M. Solvent Compatibility of Poly (dimethylsiloxane)-Based Microfluidic Devices. *Anal. Chem.* **2003**, *75*, 6544−6554.
(44) Honda, T.; Miyazaki, M.; Nakamura, H.; Maeda, H. Controllable polymerization of N-carboxy anhydrides in a microreaction system. *Lab Chip* **2005**, *5*, 812−818.
(45) Veldhuis, S. A.; George, A.; Nijland, M.; ten Elshof, J. E. Concentration Dependence on the Shape and Size of Sol-Gel-Derived Yttria-Stabilized Zirconia Ceramic Features by Soft Lithographic Patterning. *Langmuir* **2012**, *28*, 15111−15117.
(46) Dollase, W. A. Correction of Intensities for Preferred Orientation in Powder Diffractometry: Application of the March Model. *J. Appl. Crystallogr.* **1986**, *19*, 267−272.
(47) Mitzi, D. B. Solution-processed inorganic semiconductors. *J. Mater. Chem.* **2004**, *14*, 2355−2365.
(48) Einstein, A. On the Motion of Small Particles Suspended in Liquids at Rest Required by the Molecular-Kinetic Theory of Heat. *Ann. Phys.* **1905**, *17*, 549−560.
(49) Fang, H.-H.; Protesescu, L.; Balazs, D. M.; Adjokatse, S.; Kovalenko, M. V.; Loi, M. A. Exciton Recombination in Formamidinium Lead Triiodide: Nanocrystals versus Thin Films. *Small* **2017**, *13*, 1700673.
(50) Dohner, E. R.; Jaffe, A.; Bradshaw, L. R.; Karunadasa, H. I. Intrinsic White-Light Emission from Layered Hybrid Perovskites. *J. Am. Chem. Soc.* **2014**, *136*, 13154−13157.
(51) Yangui, A.; Garrot, D.; Lauret, J. S.; Lusson, A.; Bouchez, G.; Deleporte, E.; Pillet, S.; Bendeif, E. E.; Castro, M.; Triki, S.; Abid, Y.; Boukheddaden, K. Optical Investigation of Broadband White-Light Emission in Self-Assembled Organic-Inorganic Perovskite $(C_6H_{11}NH_3)_2PbBr_4$. *J. Phys. Chem. C* **2015**, *119*, 23638−23647.
(52) Yin, J.; Li, H.; Cortecchia, D.; Soci, C.; Brédas, J.-L. Excitonic and Polaronic Properties of 2D Hybrid Organic-Inorganic Perovskites. *ACS Energy Lett.* **2017**, *2*, 417−423.
(53) Kohlrausch, R. Theorie des elektrischen Rückstandes in der Leidener Flasche. *Poggendorff's Ann. Phys.* **1854**, *91*, 179−214.
(54) Alvarez, F.; Alegra, A.; Colmenero, J. Relationship between the time-domain Kohlrausch-Williams-Watts and frequency-domain Havriliak-Negami relaxation functions. *Phys. Rev. B: Condens. Matter Mater. Phys.* **1991**, *44*, 7306−7312.
(55) Zatryb, G.; Podhorodecki, A.; Misiewicz, J.; Cardin, J.; Gourbilleau, F. On the nature of the stretched exponential photoluminescence decay for silicon nanocrystals. *Nanoscale Res. Lett.* **2011**, *6*, 106.
(56) D'Innocenzo, V.; Kandada, A. R. S.; De Bastiani, M.; Gandini, M.; Petrozza, A. Tuning the Light Emission Properties by Band Gap Engineering in Hybrid Lead Halide Perovskite. *J. Am. Chem. Soc.* **2014**, *136*, 17730−17733.
(57) Ren, X.; Yang, Z.; Yang, D.; Zhang, X.; Cui, D.; Liu, Y.; Wei, Q.; Fan, H.; Liu, S. Modulating crystal grain size and optoelectronic properties of perovskite films for solar cells by reaction temperature. *Nanoscale* **2016**, *8*, 3816−3822.

DOI: 10.1021/acsami.8b02236
ACS Appl. Mater. Interfaces 2018, 10, 12878−12885